A scalar product for radiating resonant modes

Maria Paszkiewicz-Idzik,[1, 2, ∗] Lukas Rebholz,[2, ∗] Carsten Rockstuhl,[3, 2] and Ivan Fernandez-Corbaton[3]

[1]*Scientific Computing Center, Karlsruhe Institute of Technology, Kaiserstrasse 12, D-76131 Karlsruhe, Germany*
[2]*Institute of Theoretical Solid-State Physics, Karlsruhe Institute of Technology, Kaiserstrasse 12, D-76131 Karlsruhe, Germany*
[3]*Institute of Nanotechnology, Karlsruhe Institute of Technology, Kaiserstrasse 12, D-76131 Karlsruhe, Germany*

The study of the modes of optical resonators is beneficial for theoretical and practical endeavors. Here, we introduce a scalar product, originally devised for radiation fields, to such studies. This scalar product allows one to normalize and compare resonant modes using their corresponding radiation fields. Such fields are polychromatic fields free of divergences, which are determined for any given mode by its complex frequency and the modal field on the surface of the resonator. The scalar product is expressed as a surface integral involving the modal fields, multiplied by a closed-form factor incorporating the complex frequencies. In a practical application, we study the modes of disk-shaped whispering gallery resonators, and we show that the proposed scalar product accurately predicts the geometry-dependent coupling between modes.

I. INTRODUCTION AND SUMMARY

Optical resonators allow us to control and enhance light-matter interactions [1]. They offer strong optical confinement, which can reduce the size of optical instruments and decrease optical loss [2]. Resonant recirculation of an input signal increases the field intensity, which finds applications in lasers and photovoltaics [1–3]. The implementation of optical resonators differs in form, materials, and principle of operation. Among the many kinds of optical resonators, the ones hosting whispering gallery modes (WGMs) are particularly attractive for many applications due to their high quality factor and unique spectral properties such as tunability, narrow linewidth, and high stability [2, 4, 5].

The physics of resonators can be conveniently studied through their resonant modes [6], which are the natural damped resonances of the system. Such modes are also known as quasi-normal modes, leaky modes, electromagnetic eigenmodes, or simply, modes. In particular, resonant modes are being used for the study and engineering of light-matter interactions [7–22]. For example, the fields scattered by the resonator upon a given illumination may be expanded to good approximation as a linear combination of a few modal fields, at least in limited frequency ranges [23, 24]. The general question of orthogonality and completeness of the modal fields outside the resonator is particularly relevant for such applications [25]. Such a question is complicated by the divergence of time-harmonic modal fields as $|\mathbf{r}| \to \infty$, albeit, in principle, such divergence can be mitigated by causality [12, 26]. An even more fundamental question [8, 16] is *which scalar product to use for normalization and projections?*

Regarding radiated fields, there is a scalar product with many desirable properties [27]. For example, the square of the norm induced by such scalar product $\langle f|f \rangle$ gives the number of photons of the field [28]. Also, the

values of fundamental quantities in the field, such as energy or momentum, can be computed as "sandwiches" $\langle f|\Gamma|f \rangle$, where Γ is the operator representing the particular fundamental quantity [29, Chap. 3,§9]. For example, using the energy operator H, the value of $\langle f|\mathrm{H}|f \rangle$ can be shown to be identical to the typical integral giving the energy of the field. Moreover, the invariance properties of the scalar product $\langle f|g \rangle$ underpin the consistent definition of projective measurements in electromagnetism [30, Sec. III]. The use of this scalar product in light-matter interactions has been recently reviewed [31].

Here, we investigate the use of the scalar product for radiation fields in the study of optical resonators. We start by deriving a polychromatic radiation field free of divergences from the field profile and the complex frequency of a given electromagnetic eigenmode of a three-dimensional (3D) structure. Then, a cross-energy expression between the radiations of any two given eigenmodes, $\langle f|\mathrm{H}|g \rangle$, is identified as a suitable scalar product after the first obvious candidate, $\langle f|g \rangle$, is discarded because $\langle f|f \rangle$ diverges for any given eigenmode. The computation of $\langle f|\mathrm{H}|g \rangle$ consists of the integral of a simple function of the modal fields at the surface of the resonator, and a closed-form factor involving the complex modal frequencies.

We show that the cross-energy scalar product produces physically relevant information, by means of a first exemplary application. Inspired by the coupling between WGMs reported in [32], we study the coupling between the modes of a disk resonator as the thickness of the disk changes. We observe that the absolute value of $\langle f|\mathrm{H}|g \rangle$ between two normalized modes is zero when there is no interaction between them, in particular when the real frequencies of that particular pair of modes cross. In sharp contrast, for interacting anti-crossing modes, the same quantity shows a prominent peak that grows as the real frequencies of that particular pair of modes get close to each other. The position of the peak coincides with the thickness for which the two modes anti-cross, denoting interaction between modes, which here translates to non-orthogonality. We also provide evidence that strongly suggests that the height of such a peak is a measure of modal coupling strength: The peak occurs at the thick-

---

∗ These authors contributed equally.

ness that coincides with the maximum overlap of the internal modal profiles, when the energy exchange between the two modes should also be maximum. Besides our example, the studying of coupling between modes is of interest in the study of other resonant structures in the literature [33–35].

The rest of the article is organized as follows. In Section II, we first put forward a way to obtain the field radiated by a given leaky mode using causality. The resulting polychromatic field is free of divergences. We then start from a recent surface integral expression of the $\langle f|g \rangle$ scalar product, introduced in [36], and derive the corresponding expression for radiation fields of resonant modes of 3D structures. We show that $\langle f|f \rangle$ diverges, but $\langle f|\mathrm{H}|f \rangle$ does not, and we adopt the latter, which we call cross-energy scalar product. In Section III, we apply the cross-energy scalar product to the resonant modes of a disk-shaped WGM resonator, with the particular aim of studying the coupling between modes as the thickness of the disk changes. We finish with conclusions and an outlook in Section IV.

II. A SCALAR PRODUCT FOR LEAKY MODES IN 3D STRUCTURES

We start by establishing a way to obtain the field radiated by a given leaky mode. The resulting polychromatic field is free of divergences.

A. Electromagnetic fields radiated by a leaky mode

Let us consider Fig. 1, where a closed surface in $\mathbb{R}^3$ delimits a volume D with a boundary ∂D that has continuous first derivatives. It is surrounded by an achiral, non-absorbing, homogeneous, and isotropic background medium, which we assume to be vacuum for simplicity, but without loss of generality. Any other such surrounding medium can be readily accommodated in the formulas by replacing the vacuum permittivity and permeability by those of the medium. We assume the existence of time-dependent helical fields $\mathbf{F}_\lambda(\mathbf{r} \in \partial D, t)$, for helicity $\lambda = \pm 1$, on the boundary surface ∂D.

The time-dependent fields are given in SI units as

$$\mathbf{F}_\lambda(\mathbf{r}, t) = \sqrt{\frac{\varepsilon_0}{2}} \left[\mathbf{E}(\mathbf{r}, t) + \mathrm{i}\lambda Z_0 \mathbf{H}(\mathbf{r}, t) \right], \qquad (1)$$

with vacuum permittivity ε_0, vacuum impedance Z_0, time and spatially dependent complex electric field $\mathbf{E}(\mathbf{r}, t)$, and complex magnetic field $\mathbf{H}(\mathbf{r}, t)$. We also use their monochromatic components $\mathbf{F}_\lambda(\mathbf{r}, |\mathbf{k}|)$, which define the $\mathbf{F}_\lambda(\mathbf{r}, t)$ through a one-sided inverse Fourier transform:

$$\mathbf{F}_\lambda(\mathbf{r}, t) = \int_{>0}^\infty \frac{\mathrm{d}|\mathbf{k}|}{\sqrt{2\pi}} \, \mathbf{F}_\lambda(\mathbf{r}, |\mathbf{k}|) \exp(-\mathrm{i}c_0|\mathbf{k}|t), \qquad (2)$$

where $|\mathbf{k}|$ is the angular wavenumber, and c_0 denotes the speed of light in vacuum.
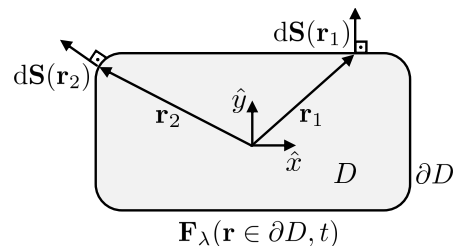

FIG. 1. A volume D in $\mathbb{R}^3$ is delimited by a closed surface ∂D with continuous first derivative. Fields $\mathbf{F}_\lambda(\mathbf{r} \in \partial D, t)$ on the surface produce electromagnetic radiation towards spatial infinity. The $\mathrm{d}\mathbf{S}(\mathbf{r})$ are outwards-pointing normal vectors of the surface element at each point $\mathbf{r} \in \partial D$. The $\hat{x}$ and $\hat{y}$ denote unit vectors in the Cartesian coordinate system.

An expression for the electromagnetic scalar product between radiation fields that only involves integrals of the fields over closed spatial surfaces was derived in recent work [36, Eq. (17)]. In particular, the $\mathbf{F}_\lambda(\mathbf{r}, |\mathbf{k}|)$ appear in the expressions for the number of photons $\langle f|f \rangle$, and energy $\langle f|\mathrm{H}|f \rangle$ of a given field $|f\rangle$, which can be computed as integrals on a closed boundary [36, Eqs. (19, 21)]:

$$\langle f|f \rangle = \sum_{\lambda = \pm 1} (-\mathrm{i}\lambda) \int_{>0}^\infty \frac{\mathrm{d}|\mathbf{k}|}{\hbar c_0 |\mathbf{k}|}$$
$$\int_{\mathbf{r} \in \partial D} \mathrm{d}\mathbf{S}(\mathbf{r}) \cdot [\mathbf{F}_\lambda^*(\mathbf{r}, |\mathbf{k}|) \times \mathbf{F}_\lambda(\mathbf{r}, |\mathbf{k}|)], \quad (3)$$

$$\langle f|\mathrm{H}|f \rangle = \sum_{\lambda = \pm 1} (-\mathrm{i}\lambda) \int_{>0}^\infty \mathrm{d}|\mathbf{k}|$$
$$\int_{\mathbf{r} \in \partial D} \mathrm{d}\mathbf{S}(\mathbf{r}) \cdot [\mathbf{F}_\lambda^*(\mathbf{r}, |\mathbf{k}|) \times \mathbf{F}_\lambda(\mathbf{r}, |\mathbf{k}|)], \quad (4)$$

with energy operator H, infinitesimal surface element $\mathrm{d}\mathbf{S}$ at the position $\mathbf{r}$, and the integral over any piecewise smooth surface ∂D enclosing a compact volume containing the sources of radiation [36].

The fact that electromagnetic fields on a boundary act as sources of radiation fields is well-known in electromagnetism (see, e.g., [37][38, Chap. 5]), with the components of the electric and magnetic fields tangential to the surface determining the whole field outside the enclosed volume. The principle that the tangential components of the electric and magnetic fields uniquely determine the radiation field outside the volume enables us to obtain the field radiated by a given leaky mode. It is important to note that the boundary ∂D does not need to be twice continuously differentiable as stated in e.g. [37], rather once continuously differentiable is enough [38, Chap. 5]. The sufficiency of being once continuously differentiable comes from the underlying fact that the Maxwell equations for helical fields contain only first-order differentials

[38, §1-2.3], and increases the class of surfaces to which the results apply from "continuous curvature" surfaces such as an ellipsoid to "continuous tangent" surfaces such as a disk with rounded corners.

Let us now assume that the boundary ∂D in Fig. 1 is the boundary of an object, and that the electromagnetic eigenmodes of the object are available to us. Such eigenmodes will, in general, be leaky, and each of those modes with finite lifetimes can be characterized by spatial field profiles $\{\boldsymbol{\mathcal{E}}(\mathbf{r}), \boldsymbol{\mathcal{H}}(\mathbf{r})\}$, and complex frequencies $\omega = \Omega - i\Gamma$, with $\{\Omega, \Gamma\} \in \mathbb{R}^+$.

We define the helical fields produced by a given leaky mode in the surface as:

$$\begin{aligned}\mathbf{F}_\lambda(\mathbf{r}, t) &= \sqrt{\frac{\varepsilon_0}{2}} \left[\boldsymbol{\mathcal{E}}(\mathbf{r}) + i\lambda Z_0 \boldsymbol{\mathcal{H}}(\mathbf{r}) \right] \exp(-i\omega t) u(t) \\ &= \mathbf{M}_\lambda(\mathbf{r}) \exp(-i\omega t) u(t),\end{aligned} \quad (5)$$

where the second line defines $\mathbf{M}_\lambda(\mathbf{r})$. The function $u(t)$ is the Heaviside step function, which represents the fact that the leaky mode has been excited at some time, which we choose to be $t = 0$. This avoids the amplification that occurs in $\mathbf{M}_\lambda(\mathbf{r}) \exp(-i\Omega t) \exp(-\Gamma t)$ for $t < 0$ while keeping the damping that occurs for $t > 0$. Moreover, and importantly, the fields $\mathbf{F}_\lambda(\mathbf{r}, |\mathbf{k}|) \exp(-ic_0|\mathbf{k}|t)$ on the right-hand side of Eq. (2) result in radiated fields that decay as $1/|\mathbf{r}|$ as $|\mathbf{r}| \to \infty$ [37, Eq. (35)], also avoiding the divergence of the modal fields as $|\mathbf{r}|$ grows. Hence, the presented strategy avoids the two unphysical exponential growths of the modal field outside the resonator, as $t \to -\infty$, and as $|\mathbf{r}| \to \infty$, which have been tied to each other by causality [26]. Here, the wavenumbers of the source fields in ∂D are always real. In contrast, identifying the complex eigenfrequency with a complex wavenumber would cause the field outside the resonator to grow exponentially as $|\mathbf{r}|$ increases.

We note that, even though the surface fields that act as sources must be defined on the surrounding medium, and $\{\boldsymbol{\mathcal{E}}(\mathbf{r}), \boldsymbol{\mathcal{H}}(\mathbf{r})\}$ are the fields inside the object, this is not a problem because the tangential components of the electric and magnetic fields are continuous at the interface between the object and the surrounding medium. The surface integrals in Eq. (3) and Eq. (4) ensure that only the components tangential to the surface affect the result.

We now want to isolate the $\mathbf{F}_\lambda(\mathbf{r}, |\mathbf{k}|)$ corresponding to Eq. (5). Applying Fourier transform to $\mathbf{F}_\lambda(\mathbf{r}, t)$, and inserting the result of Eq. (5), results in

$$\int_{-\infty}^{\infty} dt\, \mathbf{F}_\lambda(\mathbf{r}, t) \exp(ic_0 qt) =$$
$$\int_0^\infty dt\, \mathbf{M}_\lambda(\mathbf{r}) \exp(i(c_0 q - \omega)t) = \frac{i\mathbf{M}_\lambda(\mathbf{r})}{c_0 q - \omega}. \quad (6)$$

On the other hand, from equation Eq. (2), we get

$$\int_{-\infty}^{\infty} dt\, \mathbf{F}_\lambda(\mathbf{r}, t) \exp(ic_0 qt) =$$
$$\int_{>0}^{\infty} \frac{d|\mathbf{k}|}{\sqrt{2\pi}} \mathbf{F}_\lambda(\mathbf{r}, |\mathbf{k}|) \int_{-\infty}^{\infty} dt\, \exp(-ic_0(|\mathbf{k}| - q)t)$$
$$= \int_{>0}^{\infty} \frac{d|\mathbf{k}|}{\sqrt{2\pi}} \mathbf{F}_\lambda(\mathbf{r}, |\mathbf{k}|) \frac{2\pi}{c_0} \delta(|\mathbf{k}| - q)$$
$$= \frac{\sqrt{2\pi}}{c_0} \mathbf{F}_\lambda(\mathbf{r}, q) \quad (7)$$

by using $\int_{-\infty}^{\infty} \frac{dx}{2\pi} \exp(ix(a - b)) = \delta(a - b)$ in the second line of equation (7). Equating formulas (6) and (7), and replacing $q \to |\mathbf{k}|$, yields the monochromatic field components

$$\boxed{\frac{ic_0 \mathbf{M}_\lambda(\mathbf{r})}{\sqrt{2\pi}\,(c_0|\mathbf{k}| - \omega)} = \mathbf{F}_\lambda(\mathbf{r}, |\mathbf{k}|)}. \quad (8)$$

Given a 3D object, the necessary $\{\mathbf{M}_\lambda(\mathbf{r}), \omega\}$ can be obtained from software packages such as JCMsuite [39], Lumerical [40], or COMSOL [41], to name just a few.

Equation (8) results from our particular choice of temporal dependence in Eq. (5), which features the Heaviside step function $u(t)$. Such a choice is justified because the result in Eq. (8) is also reached by the analytical continuation onto the real frequency axis of the modal field at its complex frequency ω.

B. The cross-energy scalar product

If we plug Eq. (8) into Eq. (3), we quickly see that the integral with respect to the angular wavenumber $|\mathbf{k}|$, and therefore the entire result, diverges because of the $|\mathbf{k}| \to \mathbf{0}$ behavior of its integrand. Collecting all relevant terms, we find the following expression:

$$\int_{>0}^{\infty} \frac{d|\mathbf{k}|}{|\mathbf{k}|} \frac{1}{|(c_0|\mathbf{k}| - \omega)|^2}. \quad (9)$$

For small $|\mathbf{k}|$, the integrand behaves like

$$\frac{1}{|\mathbf{k}|} \frac{1}{|(c_0|\mathbf{k}| - \omega)|^2} \sim \frac{1}{|\mathbf{k}|} \frac{1}{|\omega|^2} \quad (\text{as } |\mathbf{k}| \to 0), \quad (10)$$

making Eq. (9) diverge. In contrast, $\langle f|\mathrm{H}|f\rangle$ from Eq. (4) does not diverge. Therefore, the number of photons of the radiation by a leaky mode is not well-defined, but its energy is. The cross-energy $\langle f|\mathrm{H}|g\rangle$, between arbitrary modes f and g, meets the requirements of a scalar product, which can be readily verified using the fact that the energy operator H is self-adjoint. This motivates us to use $\langle f|\mathrm{H}|g\rangle$ instead of $\langle f|g\rangle$ as the scalar product for

leaky modes. We call it the cross-energy scalar product:

$$\langle f|\mathrm{H}|g\rangle = \sum_{\lambda=\pm1} (-\mathrm{i}\lambda) \int_{>0}^{\infty} \mathrm{d}|\mathbf{k}|$$
$$\int_{\mathbf{r}\in\partial D} \mathrm{d}\mathbf{S}(\mathbf{r}) \cdot [\mathbf{F}_\lambda(\mathbf{r},|\mathbf{k}|)]^* \times \mathbf{G}_\lambda(\mathbf{r},|\mathbf{k}|)]$$
$$= \sum_{\lambda=\pm1} (-\mathrm{i}\lambda) \int_{>0}^{\infty} \mathrm{d}|\mathbf{k}| \frac{c_0^2}{2\pi(c_0|\mathbf{k}|-\omega_f^*)(c_0|\mathbf{k}|-\omega_g)}$$
$$\int_{\mathbf{r}\in\partial D} \mathrm{d}\mathbf{S}(\mathbf{r}) \cdot [\mathbf{M}_{\lambda,f}^*(\mathbf{r}) \times \mathbf{M}_{\lambda,g}(\mathbf{r})] , \quad (11)$$

where the first equality is [36, Eq. (17)], and the subscripts f, g denote the two considered modes. Appendix A shows that the result of the $\mathrm{d}|\mathbf{k}|$ integral can be obtained in closed form, with which one obtains:

$$\boxed{\begin{aligned}\langle f|\mathrm{H}|g\rangle &= \frac{\ln(-\omega_g)-\ln(-\omega_f^*)}{(\omega_f^*-\omega_g)} \frac{c_0}{2\pi} \\ &\left\{ \sum_{\lambda=\pm1} (-\mathrm{i}\lambda) \int_{\mathbf{r}\in\partial D} \mathrm{d}\mathbf{S}(\mathbf{r}) \cdot [\mathbf{M}_{\lambda,f}^*(\mathbf{r}) \times \mathbf{M}_{\lambda,g}(\mathbf{r})] \right\}\end{aligned}}$$
$$(12)$$

that significantly simplifies the numerical calculation of Eq. (11).

The fact that one needs to use a cross-energy scalar product is reminiscent of the scalar product derived from the Poynting vector for the propagating modes of waveguides [42, 43], which can be used to investigate the orthogonality between the modes [44].

In the following section, we use the cross-energy scalar product to study the coupling between the modes of a disk resonator as the thickness of the disk changes.

III. APPLICATION TO WHISPERING GALLERY RESONATORS

A. The modes

Here, we consider a WGM resonator, modeled as a disk of radius $25\,\mu\mathrm{m}$ and thickness changing from $1.8\,\mu\mathrm{m}$ to $3.1\,\mu\mathrm{m}$. The electric and magnetic fields alongside the resonance frequencies are computed with the finite element method (FEM) simulation software JCMsuite. It solves the resonant mode problem by finding electric and magnetic fields $(\boldsymbol{\mathcal{E}}_f(\mathbf{r}), \boldsymbol{\mathcal{H}}_f(\mathbf{r}))$ of the modes f and corresponding eigenvalues $\omega_f = \Omega_f - \mathrm{i}\Gamma_f$, satisfying the time-harmonic Maxwell equations in a source-free medium. The disk exhibits a rotational symmetry with respect to the z-axis, so the eigenmode computation is reduced to a two-dimensional problem in the plane $(\rho, \varphi = 0, z)$, as visualized in Fig. 2. At any point of the disk, the field of a given leaky mode (in Cartesian coordinates) obeys

$$\boldsymbol{\mathcal{E}}_f(\rho\cos\varphi, \rho\sin\varphi, z) = \mathbf{R} \cdot \boldsymbol{\mathcal{E}}_f(\rho, 0, z) \mathrm{e}^{\mathrm{i}N_\varphi^f\varphi}, \quad (13)$$

with azimuth φ, integer azimuthal mode number N_φ^f, and the rotation matrix[1] [39]

$$\mathbf{R} = \begin{bmatrix} \cos\varphi & -\sin\varphi & 0 \\ \sin\varphi & \cos\varphi & 0 \\ 0 & 0 & 1 \end{bmatrix}. \quad (14)$$

It is straightforward to show that the cross-energy scalar product between two modes of different N_φ vanishes identically: The integral in Eq. (12) would contain a term $\mathrm{e}^{\mathrm{i}(N_\varphi^g-N_\varphi^f)\varphi}$, which makes the integral over the cylindrical surface equal to zero unless $N_\varphi^g = N_\varphi^f$. Therefore, in the following, we only consider modes sharing the same azimuthal mode number $N_\varphi = 139$ (in accordance with [32]).
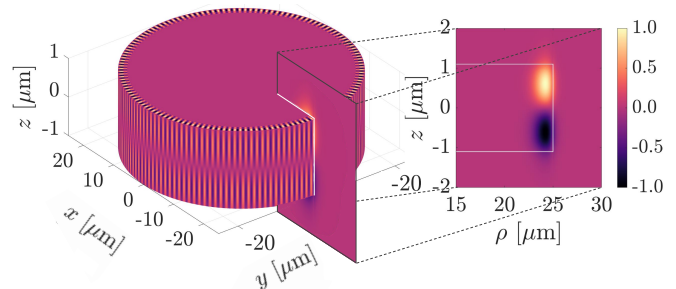

FIG. 2. The radial component of the real part of the electric field of the fundamental mode on the disk surface (left). Because of the azimuthal symmetry, we consider resonant modes computed in a slice of the disk in the xz plane (projected on the right). The discretization in the radial direction is nonuniform and finer close to the rim. The field decreases by several orders of magnitude at the borders of the chosen computational domain. For the sake of visibility, the domain in the figure differs from the size of the actual computational domain, and the scale of the z-axis is different from that of the remaining two axes.

The modes are calculated for a real permittivity $\varepsilon_{\mathrm{res}}^{\mathrm{r}} = (1.481)^2$ and imaginary permittivity $\varepsilon_{\mathrm{res}}^{\mathrm{i}} = 10^{-4}$ of the disk resonator, and the surrounding permittivity $\varepsilon_{\mathrm{sur}} = (1.000275)^2$, following [32]. Due to the field localization near the resonator rim, the region from which the fields are extracted can be limited to $[19.5, 27.0]\,\mu\mathrm{m}$ along ρ and $[-3, 3]\,\mu\mathrm{m}$ in z-direction. The target relative precision of resonance frequencies is set to 10^{-6}, and an adaptive mesh refinement scheme with two maximum refinement steps is used. The computational domain is surrounded by perfectly matched layers (PMLs) [39].

The fields $(\boldsymbol{\mathcal{E}}_f(\mathbf{r}), \boldsymbol{\mathcal{H}}_f(\mathbf{r}))$ are used to construct the (helical) modal fields $\mathbf{M}_\lambda(\mathbf{r})$ according to their definition in Eq. 5. Note that the surrounding medium here is not vacuum as assumed before. However, $\varepsilon_{\mathrm{sur}}$ differs only marginally from unity and we can neglect its influence,

----

[1] Note, that JCMsuite uses a different convention with the y-axis being the axis of rotational symmetry.

since the results are essentially identical to the vacuum case.

The resonance frequencies of the modes change with varying thickness of the disk. The real parts of the frequencies of the first ten modes emerging from FEM computation are plotted in Fig. 3 for disk thicknesses ranging from 1.8 μm to 3.1 μm. As a result of FEM computation, the modes are sorted and assigned a spectral order number according to their increasing real part of the resonance frequency independently for every disk thickness. However, it is known from symmetry analysis in [32] that some modes over the course of the varying disk thickness exhibit crossings, and some exhibit avoided crossings, also called anti-crossings. In particular, the disk is invariant under the mirror reflection $z \mapsto -z$, and the field distribution $\boldsymbol{\mathcal{E}}_f(\mathbf{r})$ of each mode is an eigenstate of such reflection with eigenvalue $m_z = 1$ or $m_z = -1$, which we call the *parity* of the mode. For example, the field in Fig. 2 transforms with an eigenvalue $m_z = -1$. Note that the magnetic field distribution $\boldsymbol{\mathcal{H}}_f(\mathbf{r})$ is also an eigenstate of the reflection $z \mapsto -z$ with eigenvalue $-m_z$. Modes of opposite parity cross, indicating the lack of interaction between them, and modes with the same parity anti-cross, indicating that the modes couple and interact with each other [32]. The anti-crossings are marked with gray circles in Fig. 3. Examples of fields $\mathbf{M}_\lambda(\mathbf{r})$ associated with crossing and anti-crossing modes are presented in Fig. 8 and Fig. 9, respectively, in Appendix B. It is important to highlight that crossings affect the ordering of the modes. The spectral order coming from the numerical tool naturally swaps the labels for modes that cross as the thickness of the disk increases, and, therefore, does not reflect their true order. In our case, however, this can be circumvented by considering the spectral order of modes separately for different m_z, since crossings only occur between modes of opposite m_z.

B. The cross-energy scalar product for measuring the coupling between modes

We analyze the orthogonality properties of the modes as a function of the disk thickness using the following quantity:

$$|\langle \hat{f}|\mathrm{H}|\hat{g}\rangle|^2 = \frac{|\langle f|\mathrm{H}|g\rangle|^2}{\langle f|\mathrm{H}|f\rangle \langle g|\mathrm{H}|g\rangle}, \qquad (15)$$

where the normalization of each mode is considered so that each normalized mode radiates the same amount of energy.

The integral in Eq. (12) is further simplified by exploiting the cylindrical symmetry of the system, which reduces the two-dimensional surface integral to a one-dimensional contour integral. See Appendix A for details. The integral is then computed using the trapezoidal rule over the contour $\mathcal{C}$ drawn with a white line in the projection in Fig. 2. We chose the dimensions of the contour (the height and width) to be 2 % bigger than the actual
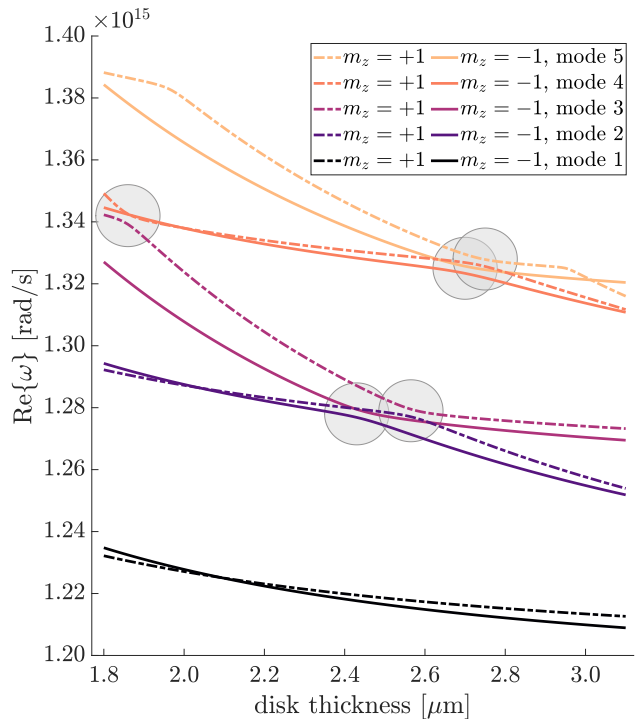

FIG. 3. Real part of the angular resonance frequency of the five pairs of lowest order modes as a function of disk thickness. Modes of equal parity m_z undergo avoided crossings at the spots marked with gray circles. Solid lines follow modes with negative parity, and dashed lines mark the resonance frequencies of modes with positive parity upon a $z \mapsto -z$ mirror transformation.

contour of the $\varphi = 0$ slice of the disk to avoid regions of numerical artifacts in the simulated fields, which are found near the sharp edges of the disk resonator. Sampling the fields slightly outside the resonator technically means sampling fields that feature an exponentially divergent behavior towards spatial infinity due to being associated with a complex wavenumber. However, the rate of divergence is related to the radiative damping of the resonant modes. For fairly high-quality resonances, indicated by the ratio Ω/Γ, in the order of 10^5 for the modes discussed here, the exponential divergence is slow enough to be negligible close to the resonator surface. Correspondingly, this is a close approximation to the desired fields at the surface of the disk. The contour is discretized finer close to the rim of the disk, where the fields are localized. While the sampling points are chosen to coincide with the contour of a resonator with sharp edges, this does not violate the assumption of "continuous tangent" surfaces pointed out earlier since the contour's region of curvature can be assumed small compared to the finite sampling.

The modes that cross, having opposite parity, are orthogonal under the cross-energy scalar product. This is readily seen by splitting the surface integral in Eq. (12) into its $z > 0$ and $z < 0$ pieces, whose sum cancels out if
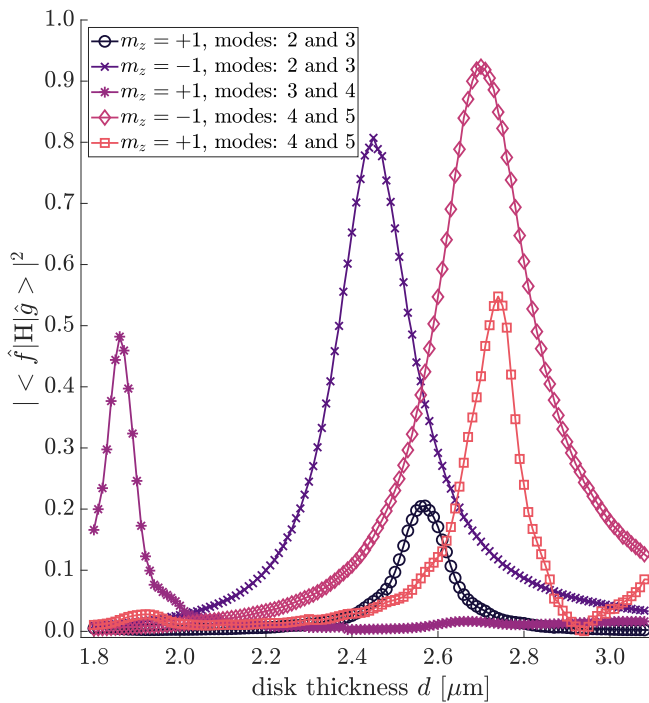
FIG. 4. Result of Eq. (15) for chosen pairs of modes as a function of disk thickness. The peaks coincide with the thickness for which the anti-crossing occurs between the particular modes, as marked in Fig. 3.
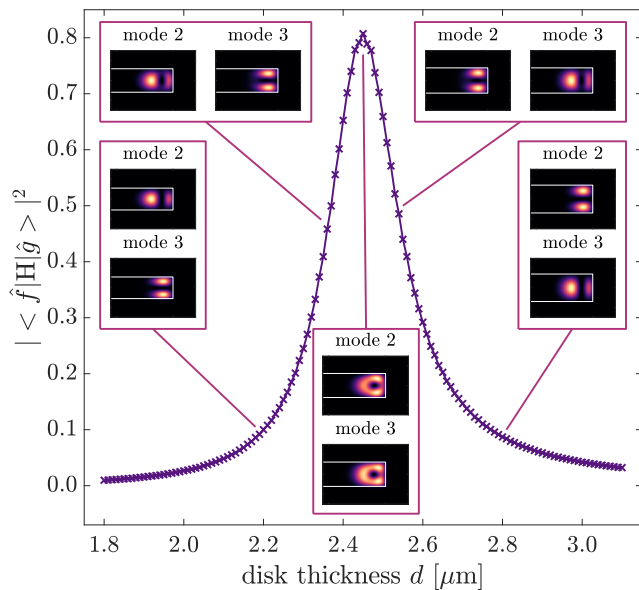

FIG. 5. Result of Eq. (15) for the modes of spectral order 2 and 3 and parity $m_z = -1$ as a function of the disk thickness. The inset figures show the normalized energy density distribution of the modes at particular values of the thickness. The field distributions plotted here are closely related to the ones in [32, Fig. 3].

the modes have opposite parity. Figure 4 shows the result of Eq. (15) for selected pairs of modes of the same parity. Each line shows how a prominent peak grows as the real frequencies of that particular pair of modes get close to each other in Fig. 3. The position of the peak neatly aligns with the thicknesses at which the two modes anti-cross, denoting interaction between modes, which here translates into enlarged non-orthogonality. We surmise that the height of each peak is a measure of modal coupling strength. Such a possibility is strongly suggested by the results in Fig. 5, which shows the value of Eq. (15) for a pair of modes of $m_z = -1$. The inset figures present the electric field density profiles of the investigated modes for chosen values of disk thickness. As the disk thickness increases, the profiles deform, reach approximately the same shape and overlap, and then separate but with interchanged modal numbers $(2,3) \leftrightarrow (3,2)$. The cross-energy scalar product peaks exactly when the two mode profiles have maximum overlap, and hence when the maximum coupling between them in terms of energy exchange is expected.

IV. CONCLUSION AND OUTLOOK

We have put forward a scalar product for the study of optical resonators. We showed how any given numerical resonant mode obtained from a Maxwell solver can be used to determine fields on the surface of the resonator that produce a polychromatic radiation free of divergences. Then, we identified a cross-energy expression between the radiations of any two given eigenmodes as a suitable scalar product. The application to the modes of a disk-shaped WGM resonator showed that the cross-energy scalar product produces physically relevant information, as it predicts the coupling between modes upon smooth changes of the geometrical parameters of the disk.

The same cross-energy scalar product can be used between the radiation of a given eigenmode and any general radiation field, thereby allowing the decomposition of the latter into normalized eigenmodes. This scalar product also opens a path for a different elucidation of the orthogonality and degree of asymptotic completeness of a given series of resonant modes. Moreover, one may always derive an orthonormal set of modes from the possibly non-orthogonal set produced by numerical solvers.

We also envision the use of the cross-energy scalar product between eigenmodes as a general way to track such modes, as some resonator parameters change smoothly. This can be done by projecting the radiation field of each mode for a given set of parameters onto the radiation field of each mode in the next set and connecting a given mode of the first set to the mode of the second set which results in the maximum value of the projection. In our application to a disk, such mode tracking can be performed "manually" using symmetry arguments, but more complex resonators may not allow it.

ACKNOWLEDGEMENTS

Appendix A: Cross-energy scalar product

1. A general simplification

The formula for the cross-energy scalar product in Eq. (11) reads

$$
\langle f|\mathrm{H}|g\rangle = \sum_{\lambda=\pm 1} \int_{>0}^{\infty} \mathrm{d}|\mathbf{k}| \frac{-\mathrm{i}\lambda c_0^2}{2\pi(c_0|\mathbf{k}|-\omega_f^*)(c_0|\mathbf{k}|-\omega_g)}
$$
$$
\int_{\mathbf{r}\in\partial D} \mathrm{d}\mathbf{S}(\mathbf{r})\cdot\left[\mathbf{M}_{\lambda,f}^*(\mathbf{r})\times\mathbf{M}_{\lambda,g}(\mathbf{r})\right] , \quad (A1)
$$

with subscripts f, g denoting two considered resonant modes. Calculating the scalar product Eq. (A1) numerically over the whole 3D object requires either vast computing resources or much time. However, the integral over $|\mathbf{k}|$ can be solved analytically and reads

$$
\int_{>0}^{\infty} \frac{\mathrm{d}|\mathbf{k}|}{(c_0|\mathbf{k}|-\omega_f^*)(c_0|\mathbf{k}|-\omega_g)} = \frac{\ln(-\omega_g)-\ln(-\omega_f^*)}{c_0(\omega_f^*-\omega_g)} .
$$
$$
(A2)
$$

The real and imaginary parts of the resulting function are plotted separately for an exemplary pair of anti-crossing modes in Fig. 6.

2. Application to a disk

In our example, the surface integral in Eq. (A1) can be rewritten to

$$
\int_{\mathbf{r}\in\partial D} \mathrm{d}\mathbf{S}(\mathbf{r})\cdot\left[\mathbf{M}_{\lambda,f}(\mathbf{r})^*\times\mathbf{M}_{\lambda,g}(\mathbf{r})\right]
$$
$$
= 2\pi\int_{\mathcal{C}} \mathrm{d}s\rho\hat{\mathbf{v}}(\mathbf{r})\cdot\left[\mathbf{M}_{\lambda,f}(\mathbf{r})^*\times\mathbf{M}_{\lambda,g}(\mathbf{r})\right] , \quad (A3)
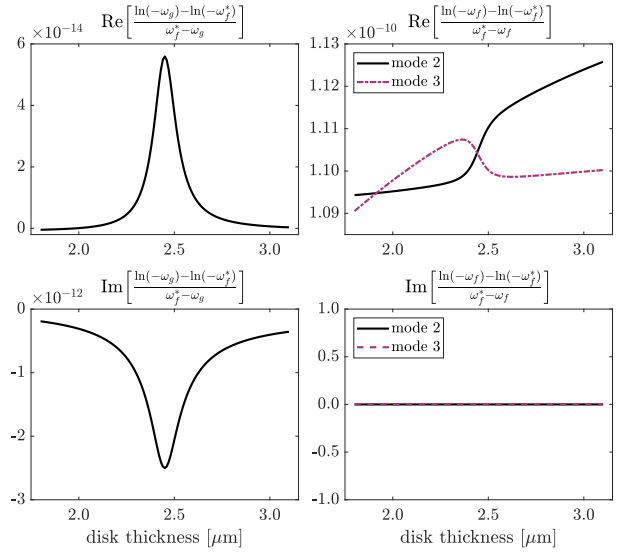$$

FIG. 6. Real and imaginary parts of the integral over $|\mathbf{k}|$ for two anti-crossing modes of $m_z = -1$ (left column), and the modes with themselves (right column).

taking into account the cylindrical symmetry of the surface ∂D and Eq. (13), and writing $\mathrm{d}\mathbf{S}(\mathbf{r}) = \mathrm{d}s\cdot\rho\mathrm{d}\varphi\hat{\mathbf{v}}(\mathbf{r})$ in cylindrical coordinates (ρ,φ,z), with the surface normal vector $\hat{\mathbf{v}}$. The fields $\mathbf{M}_{\lambda,f}(\mathbf{r})$ and $\mathbf{M}_{\lambda,g}(\mathbf{r})$ are taken from the FEM solver. Here, $\mathcal{C}$ refers to the 1D curve defined at the $\varphi = 0$ slice of ∂D, and $\mathrm{d}s$ denotes a differential line element of $\mathcal{C}$. The $\mathrm{d}\varphi$ integral has been carried out explicitly and results in the prefactor of 2π. The values of the integral in Eq. (A3) summed for both helicities as a function of disk thickness are plotted in Fig. 7.
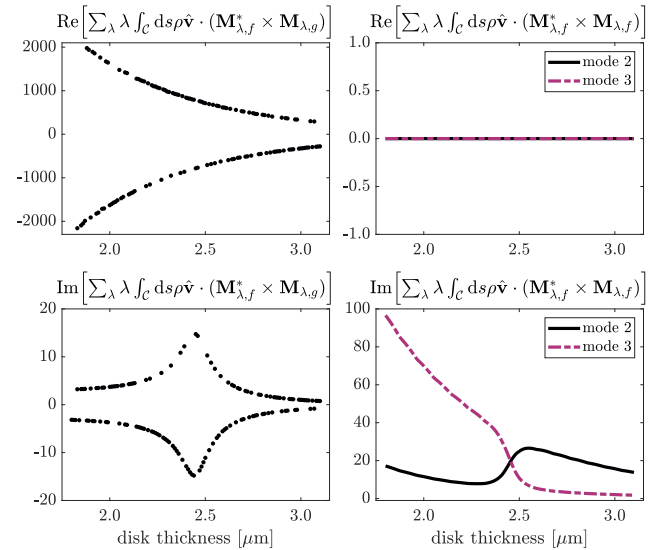

FIG. 7. Real and imaginary part of contour integral of two anti-crossing modes of $m_z = -1$ (left column), and the modes with themselves (right column).

It is important to note that the actual values plotted

in Fig. 7 are not physically meaningful since they depend on the normalization scheme of the Maxwell solver used to obtain the modal fields, JCMsuite in this case. In principle, the numerically obtained modal fields ($\boldsymbol{\mathcal{E}}_f(\mathbf{r})$, $\boldsymbol{\mathcal{H}}_f(\mathbf{r})$) scaled by an arbitrary (complex) factor are still a valid solution to the resonance problem. A consequence of this is directly observed in the left column of Fig. 7: The applied normalization scheme apparently allows for relative changes in sign between modes evaluated at different disk thicknesses. This does not happen simultaneously for all modes and leads to seemingly random changes in the overall sign of the scalar product, seen by the symmetric distribution of values around the x-axis in the left column. This does not affect the data shown in the main text since we only consider absolute values of the normalized scalar product in Eq. (15).

Combining all simplifications, the final formula for the scalar product reads

$$
\begin{aligned}
\langle f|\mathrm{H}|g\rangle = \sum_{\lambda=\pm 1} (-\mathrm{i}\lambda c_0)\frac{\ln(-\omega_g) - \ln(-\omega_f^*)}{\omega_f^* - \omega_g} \\
\int_{\mathcal{C}} \mathrm{d}s\rho\hat{\mathbf{v}}(\mathbf{r}) \cdot [\mathbf{M}_{\lambda,f}(\mathbf{r})^* \times \mathbf{M}_{\lambda,g}(\mathbf{r})] \, . \quad \text{(A4)}
\end{aligned}
$$

Appendix B: Exemplary mode profiles

In Fig. 8, we show the Cartesian components of the mode profiles $\mathbf{M}_\lambda(\rho, z)$ of the fundamental (spectral order number 1) modes, for $\lambda = +1$, characterized by different parities m_z. Modes of different symmetry eigenvalue are orthogonal to each other and do not couple. Therefore, the integral in Eq. (12) over the surface of the disk vanishes (up to numeric imprecision).

In Fig. 9, we show the Cartesian components of the mode profiles of $\mathbf{M}_\lambda(\rho, z)$ of the second and the third

mode of equal parities $m_z = -1$. Since the modes share the same eigenvalue upon mirror transformation $z \mapsto -z$, mode coupling is not prohibited by symmetry.
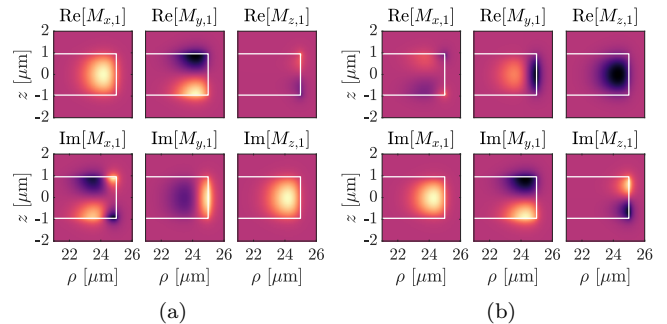

FIG. 8. Cartesian components of the real (upper row) and imaginary (bottom row) part of the field $\mathbf{M}$ of the first modes, characterized by (a) $m_z = +1$ and (b) $m_z = -1$.
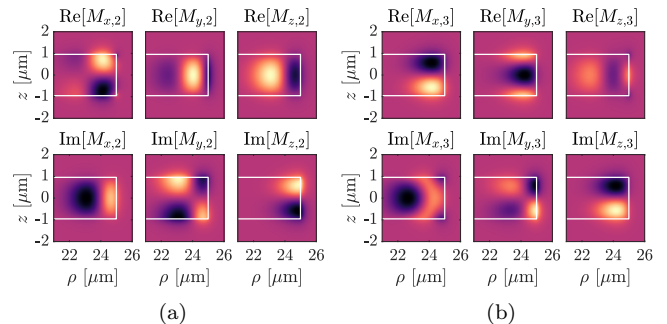

FIG. 9. Cartesian components of the real (upper row) and imaginary (bottom row) part of the field $\mathbf{M}$ of the (a) second and the (b) the third mode, both characterized by $m_z = -1$.

[1] K. J. Vahala, Optical microcavities, Nature **424**, 839 (2003).

[2] Z. Yuan, P. C. Wu, and Y.-C. Chen, Optical resonator enhanced photovoltaics and photocatalysis: fundamental and recent progress, Laser Photonics Rev. **16**, 2100202 (2022).

[3] Y. Zhang, Z. Yuan, Z. Qiao, D. Barshilia, W. Wang, G.-E. Chang, and Y.-C. Chen, Tunable microlasers modulated by intracavity spherical confinement with chiral liquid crystal, Adv. Opt. Mater. **8**, 1902184 (2020).

[4] V. S. Ilchenko and A. B. Matsko, Optical resonators with whispering-gallery modes-part II: applications, IEEE J. Sel. Top. Quantum Electron. **12**, 15 (2006).

[5] M. Loyez, M. Adolphson, J. Liao, and L. Yang, From whispering gallery mode resonators to biochemical sensors, ACS Sens. **8**, 2440 (2023).

[6] P. T. Kristensen, K. Herrmann, F. Intravaia, and K. Busch, Modeling electromagnetic resonators using quasinormal modes, Adv. Opt. Photonics **12**, 612 (2020).

[7] P. Lalanne, W. Yan, A. Gras, C. Sauvan, J.-P. Hugonin, M. Besbes, G. Demésy, M. D. Truong, B. Gralak, F. Zolla, A. Nicolet, F. Binkowski, L. Zschiedrich, S. Burger, J. Zimmerling, R. Remis, P. Urbach, H. T. Liu, and T. Weiss, Quasinormal mode solvers for resonators with dispersive materials, J. Opt. Soc. Am. A **36**, 686 (2019).

[8] C. Sauvan, T. Wu, R. Zarouf, E. A. Muljarov, and P. Lalanne, Normalization, orthogonality, and completeness of quasinormal modes of open systems: the case of electromagnetism, Opt. Express **30**, 6846 (2022).

[9] R.-C. Ge and S. Hughes, Quantum dynamics of two quantum dots coupled through localized plasmons: An intuitive and accurate quantum optics approach using quasinormal modes, Phys. Rev. B **92**, 205420 (2015).

[10] M. Kamandar Dezfouli and S. Hughes, Regularized quasi-normal modes for plasmonic resonators and open cavities, Phys. Rev. B **97**, 115302 (2018).

[11] F. Binkowski, F. Betz, R. Colom, M. Hammerschmidt, L. Zschiedrich, and S. Burger, Quasinormal mode expansion of optical far-field quantities, Phys. Rev. B **102**, 035432 (2020).

[12] R. Colom, R. McPhedran, B. Stout, and N. Bonod, Modal expansion of the scattered field: Causality, non-divergence, and nonresonant contribution, Phys. Rev. B **98**, 085418 (2018).

[13] T. Wu, M. Gurioli, and P. Lalanne, Nanoscale light confinement: the Q's and V's, ACS Photonics **8**, 1522 (2021).

[14] R.-C. Ge, P. T. Kristensen, J. F. Young, and S. Hughes, Quasinormal mode approach to modelling light-emission and propagation in nanoplasmonics, New J. Phys. **16**, 113048 (2014).

[15] M. V. Gorkunov, A. A. Antonov, A. V. Mamonova, E. A. Muljarov, and Y. Kivshar, Substrate-induced maximum optical chirality of planar dielectric structures, Adv. Opt. Mater. , 2402133 (2024).

[16] P. T. Kristensen, C. Van Vlack, and S. Hughes, Generalized effective mode volume for leaky optical cavities, Opt. Lett. **37**, 1649 (2012).

[17] S. Franke, S. Hughes, M. K. Dezfouli, P. T. Kristensen, K. Busch, A. Knorr, and M. Richter, Quantization of quasinormal modes for open cavities and plasmonic cavity quantum electrodynamics, Phys. Rev. Lett. **122**, 213901 (2019).

[18] N. A. Gippius, T. Weiss, S. G. Tikhodeev, and H. Giessen, Resonant mode coupling of optical resonances in stacked nanostructures, Opt. Express **18**, 7569 (2010).

[19] T. Coenen, J. Van De Groep, and A. Polman, Resonant modes of single silicon nanocavities excited by electron irradiation, ACS Nano **7**, 1689 (2013).

[20] D. Martin-Cano, H. R. Haakh, and N. Rotenberg, Chiral emission into nanophotonic resonators, ACS Photonics **6**, 961 (2019).

[21] T. Wu and P. Lalanne, Exact maxwell evolution equation of resonator dynamics: temporal coupled-mode theory revisited, Opt. Express **32**, 20904 (2024).

[22] F. Betz, M. Hammerschmidt, L. Zschiedrich, S. Burger, and F. Binkowski, Efficient rational approximation of optical response functions with the AAA algorithm, Laser Photonics Rev. , 2400584 (2024).

[23] J. Ren, S. Franke, and S. Hughes, Connecting classical and quantum mode theories for coupled lossy cavity resonators using quasinormal modes, ACS Photonics **9**, 138 (2022).

[24] M. Kamandar Dezfouli and S. Hughes, Quantum optics model of surface-enhanced raman spectroscopy for arbitrarily shaped plasmonic resonators, ACS Photonics **4**, 1245 (2017).

[25] S. Both and T. Weiss, Resonant states and their role in nanophotonics, Semicond. Sci. Technol. **37**, 013002 (2021).

[26] M. I. Abdelrahman and B. Gralak, Completeness and divergence-free behavior of the quasi-normal modes using causality principle, OSA Contin. **1**, 340 (2018).

[27] L. Gross, Norm invariance of Mass-Zero equations under the conformal group, J. Math. Phys. **5**, 687 (1964).

[28] Y. B. Zel'dovich, The number of quanta as an invariant of classical electromagnetic field, Proc. USSR Acad. Sci. **163**, 1359 (1965).

[29] I. Bialynicki-Birula and Z. Bialynicka-Birula, *Quantum Electrodynamics* (Pergamon, Oxford, UK, 1975).

[30] I. Fernandez-Corbaton and M. Vavilin, A scalar product for computing fundamental quantities in matter, Symmetry **15**, 1839 (2023).

[31] I. Fernandez-Corbaton, An algebraic approach to light–matter interactions, Adv. Phys. Res. , 2400088 (2024).

[32] S. Woska, L. Rebholz, P. Rietz, and H. Kalt, Intrinsic mode coupling in mirror-symmetric whispering gallery resonators, Opt. Express **30**, 32847 (2022).

[33] X. Wang, Z. Wang, H. Dong, C. N. Saggau, H. Tang, M. Tang, L. Liu, S. Baunack, L. Bai, J. Liu, *et al.*, Collective coupling of 3D confined optical modes in monolithic twin microtube cavities formed by nanomembrane origami, Nano Lett. **22**, 6692 (2022).

[34] A. Kameda, S. Shimomoto, H. Tajima, J.-i. Yamada, T. Yokomatsu, K. Maenaka, and T. Komino, Mode coupling of whispering gallery modes through organic semiconductor thin films, J. Phys. Chem. C **125**, 14940 (2021).

[35] C. Klusmann, J. Oppermann, P. Forster, C. Rockstuhl, and H. Kalt, Identification of dielectric, plasmonic, and hybrid modes in metal-coated whispering-gallery-mode resonators, ACS Photonics **5**, 2365 (2018).

[36] M. Vavilin, C. Rockstuhl, and I. Fernandez-Corbaton, Electromagnetic scalar product in spatially bounded domains, Phys. Rev. A **109**, 043506 (2024).

[37] R. Kress, *Scattering*, edited by E. Pike and P. C. Sabatier (Academic Press, London, 2001).

[38] A. Lakhtakia, *Beltrami fields in chiral media* (World Scientific, 1994).

[39] JCMwave GmbH Berlin, *JCMsuite Documentation*, https://www.jcmwave.com/docs/ParameterReference/ (2019).

[40] Lumerical Inc, *MODE: Waveguide Simulator*, https://www.lumerical.com/ (2024).

[41] COMSOL Inc, *COMSOL Multiphysics Reference Manual, version 5.3*, www.comsol.com (2024).

[42] K. Hiremath, M. Hammer, R. Stoffer, L. Prkna, and J. Čtyroký, Analytic approach to dielectric optical bent slab waveguides, Opt. Quantum Electron. **37**, 37 (2005).

[43] K. Hiremath, R. Stoffer, and M. Hammer, Modeling of circular integrated optical microresonators by 2-d frequency domain coupled mode theory, Opt. Commun. **257**, 277 (2006).

[44] M. Paszkiewicz, M. Sukhova, W. Dörfler, and C. Rockstuhl, Approximation method for fast calculation of transmission in multi-mode waveguides, J. Opt. Soc. Am. A **41**, 174 (2024).